

GENERATION OF SEED MAGNETIC FIELD AROUND FIRST STARS: EFFECTS OF RADIATION FORCE

MASASHI ANDO¹, KENTARO DOI², AND HAJIME SUSA³
 Department of Physics, Konan University, Okamoto, Kobe, Japan
Draft version June 4, 2010

ABSTRACT

We investigate seed magnetic field generation in the early universe by radiation force of first stars. In a previous study with the steady assumption, large amplitudes ($\sim 10^{-15}$ G for first stars, $\sim 10^{-11}$ G for QSOs) are predicted. In this study, we formulate this issue in an unsteady framework. Then, we consider a specific model of magnetic field generation around a very massive first star. Consequently, we (1) find that the steady assumption is not valid in realistic situations, and (2) obtain much smaller magnetic field strength than predicted by Langer et al. In addition, we find that the momentum transfer process during photoionization is more important than Thomson scattering. The resultant magnetic flux density around the first star is $\lesssim 10^{-19}$ G. This seed magnetic field will not affect subsequent star formation in the neighborhood of first stars.

Subject headings: early universe—HII regions—magnetic fields—radiative transfer

1. INTRODUCTION

One of the most important current issues in cosmology is understanding the star formation history of the universe, especially the early universe. Owing to progress in the last decade, mainly due to theoretical studies, we now expect the very first stars in the early universe to be very massive ($\gtrsim 100M_{\odot}$), compared to those in present-day galaxies (e.g., Bromm, Coppi & Larson 2002; Nakamura & Umemura 2001; Abel, Bryan, Norman 2002; Yoshida 2006).

The chief reason that the first stars are very massive is the lack of heavy elements in the primordial gas, since the heavy elements are efficient coolants. Theoretical studies suggest that when the metallicity of the star forming gas exceeds 10^{-5} to $10^{-6}Z_{\odot}$, the star formation mode transits from very massive star formation to normal star formation (Schneider et al. 2003; Omukai et al. 2005). Thus, metallicity is the key factor for the transition of the star formation mode.

Another possible parameter is magnetic field strength. In the present-day star-forming molecular cloud, energy density of the magnetic field is comparable to gravitational or turbulent energy density, while it is assumed that the magnetic field is weak in the primordial gas. Magnetic field in present-day galaxies basically suppresses the star formation process.

The effects of magnetic field on the early star formation episode in the universe have been studied by several authors. The coupling between magnetic field and pure primordial gas has been investigated (Maki & Susa 2004, 2007). They found that the magnetic field is always frozen in the gas in so far as the magnetic field strength is not strong enough to prevent gravitational contraction. Based on the frozen-in assumption, it is found that bipolar outflows emerge in cases $B > 10^{-9}$ G is satisfied at $n_{\text{H}} = 10^3 \text{ cm}^{-3}$ (Machida et al. 2006). Tan & Blackman (2004) suggest that magnetorotational Instability (MRI) is activated in the accretion disk surrounding proto first stars in cases where $B > 10^{-10}$ G at $n_{\text{H}} = 10^3 \text{ cm}^{-3}$, which results in efficient angular momentum transfer in the disk. It is also reported by Schleicher et al. (2009) that gravitational contraction of the primordial gas is delayed in cases where the comoving field strength is larger than 10^{-10} G.

Therefore, it is crucial to determine the magnetic field strength that exists in the environment of the star-forming gas cloud in the early universe in order to understand the transition of the star formation mode. Magnetic field strength at the star formation site in the early universe is basically provided by the field generated prior to nonlinear structure formation (e.g., Harrison 1970; Mishustin & Ruzmaikin 1972; Turner & Widrow 1988; Ichiki et al. 2006), as well as the field generated by the Biermann battery effect (Biermann 1950) during the structure formation (e.g., Xu et al. 2008) or reionization (Gnedin et al. 2000). The predicted field strength in these models is within the range of 10^{-16} G to 10^{-20} G, which is too weak to affect star formation. Another possibility is that the magnetic field spewed out from the formed stars (e.g., Bisnovatyi-Kogan et al. 1973). In cases where the field strength is as large as ~ 1 G like normal stars, a simple flux freezing assumption again leads to $\sim 10^{-16}$ G at intergalactic medium (IGM) densities.

On the other hand, Langer et al. (2003) suggest a mechanism to generate a large amplitude of seed magnetic field as large as 10^{-11} G, which could affect the star formation in the early universe. They consider HII regions formed by luminous sources like QSOs or first stars. The radiation force field due to the photons emitted by these objects is anisotropic because of the clumpiness of surrounding media. This anisotropy causes charge separation in the HII region, which generates a large scale eddy current as well as the magnetic fields. However, the assumption in this theory is idealized. In their theory, anisotropy of radiation is dealt with as perturbation, and the HII region is assumed to be steady. In reality, dense shadows are generated behind the nearby dense halos. In addition, HII regions formed by QSOs or first stars are actually

¹ a03cb004z@gmail.com

² mn921009@center.konan-u.ac.jp

³ susa@konan-u.ac.jp

unsteady, and ionization fronts never reach the Strömgren radius (Shapiro & Giroux 1987; Kitayama et al. 2004; Yoshida et al. 2007).

In this paper, we investigate this magnetic field generation process by radiation force in nonlinear and unsteady framework along the lines of theory of Langer et al. (2003). We consider a specific model of magnetic field generation around a very massive first star and assess whether the generated magnetic field affects the subsequent star formation.

In Section 2, we describe the basic equations. A brief description and the setup of our models are described in Section 3. In Section 4, we show the results of our calculation, and Section 5 is devoted to discussion. Finally, in Section 6, we conclude our research.

2. BASIC EQUATIONS

2.1. Magnetic field generation

In this section, we describe the basic equations of magnetic field generation. To begin with, the force balance on a single electron is written as follows:

$$0 = -e\mathbf{E} + \frac{e}{\sigma_c}\mathbf{j} + \mathbf{f}_{\text{rad}} - \frac{\nabla p_e}{n_e} - \frac{e}{c}\mathbf{v}_e \times \mathbf{B} \quad (1)$$

Here, e , \mathbf{E} , \mathbf{B} , and \mathbf{j} denote the elementary charge, electric field strength, magnetic flux density, and electric current density, respectively. p_e , n_e , and \mathbf{v}_e represent the pressure, number density and velocity of electrons as fluid, respectively. σ_c is the conductivity and \mathbf{f}_{rad} is the radiation force on an electron.

The fluid velocity \mathbf{v} is defined as

$$\mathbf{v} \equiv \frac{n_p m_p \mathbf{v}_p + n_e m_e \mathbf{v}_e}{n_p m_p + n_e m_e} \simeq \mathbf{v}_p \quad (2)$$

where n_p , m_p , m_e , and \mathbf{v}_p denote the number density of protons, the mass of protons, the mass of electrons, and the velocity of protons, respectively. Thus, the velocity of electrons is approximated as $\mathbf{v}_e \simeq \mathbf{v} - \mathbf{j}/(en_e)$. Substituting this notation into Equation(1), we obtain

$$0 = -e\mathbf{E} + \frac{e}{\sigma_c}\mathbf{j} + \mathbf{f}_{\text{rad}} - \frac{\nabla p_e}{n_e} - \frac{e}{c}\mathbf{v} \times \mathbf{B} + \frac{1}{cn_e}\mathbf{j} \times \mathbf{B} \quad (3)$$

Since we consider the expanding HII region around a first star, we have to solve the following photoionization rate equation for electrons.

$$\frac{\partial n_e}{\partial t} + \nabla \cdot (n_e \mathbf{v}_e) = \Gamma - \alpha n_e n_p \quad (4)$$

Combining Equation (4) with the similar equation for protons, we obtain the charge conservation equation

$$\frac{\partial \rho}{\partial t} + \nabla \cdot \mathbf{j} = 0, \quad (5)$$

where charge density ρ and current density \mathbf{j} are related to the number density of electrons and protons as $\rho \equiv e(n_p - n_e)$ and $\mathbf{j} \equiv e(n_p \mathbf{v}_p - n_e \mathbf{v}_e)$. We also need the set of Maxwell equations:

$$\nabla \cdot \mathbf{E} = 4\pi\rho, \quad \nabla \times \mathbf{E} = -\frac{1}{c}\frac{\partial \mathbf{B}}{\partial t}, \quad \nabla \cdot \mathbf{B} = 0, \quad \nabla \times \mathbf{B} = \frac{4\pi}{c}\mathbf{j} + \frac{1}{c}\frac{\partial \mathbf{E}}{\partial t} \quad (6)$$

Equations (3),(4),(5) and (6) combined with hydrodynamic equations are the fundamental equations for this problem.

In order to obtain the equation that describes the growth of magnetic flux density, we apply $-(4\pi\sigma_c/ec)\nabla \times$ to both sides of Equation (3). We have

$$0 = -\frac{4\pi}{c}\nabla \times \mathbf{j} + \frac{4\pi\sigma_c}{c}\nabla \times \mathbf{E} + \frac{4\pi\sigma_c}{c^2}\nabla \times (\mathbf{v} \times \mathbf{B}) - \frac{4\pi\sigma_c}{c^2}\nabla \times \left(\frac{\mathbf{j} \times \mathbf{B}}{n_e} \right) - \frac{4\pi\sigma_c}{cen_e^2}\nabla n_e \times \nabla p_e - \frac{4\pi\sigma_c}{ce}\nabla \times \mathbf{f}_{\text{rad}}$$

Using the second and fourth equations of Maxwell Equations (6), we have

$$\frac{1}{c^2}\frac{\partial^2 \mathbf{B}}{\partial t^2} - \nabla^2 \mathbf{B} + \frac{4\pi\sigma_c}{c^2}\frac{\partial \mathbf{B}}{\partial t} = \frac{4\pi\sigma_c}{c^2}\nabla \times (\mathbf{v} \times \mathbf{B}) - \frac{4\pi\sigma_c}{c^2}\nabla \times \left(\frac{\mathbf{j} \times \mathbf{B}}{en_e} \right) - \frac{4\pi\sigma_c}{cen_e^2}\nabla n_e \times \nabla p_e - \frac{4\pi\sigma_c}{ce}\nabla \times \mathbf{f}_{\text{rad}} \quad (7)$$

In this expression, $4\pi\sigma_c$ denotes the inverse of the timescale that describes the convergence of electron velocity to the terminal velocity. This timescale is quite short, since $\sigma_c \simeq 6.5 \times 10^6 T^{3/2} \text{e.s.u.}$ (Lang 1999). It is as short as a picosecond in cases where we consider photoionized gas. Thus, the first and second terms on the left-hand side of the above equation are negligible compared to the third term, since the typical timescale is the lifetime of the source star which is as long as Myr, and the typical length scale is kpc. Finally, we obtain

$$\frac{\partial \mathbf{B}}{\partial t} = \nabla \times (\mathbf{v} \times \mathbf{B}) - \frac{c}{en_e^2}\nabla n_e \times \nabla p_e - \frac{c}{e}\nabla \times \mathbf{f}_{\text{rad}} \quad (8)$$

Here we also omitted the Hall current term which is proportional to $\mathbf{j} \times \mathbf{B}$, since this is a higher order term than the others, in cases where we consider the generation of very weak magnetic field. The first term on the right-hand side

denotes the advection term. If the second and third terms are neglected, the frozen-in condition is satisfied. The second term describes the well-known Biermann battery term (Biermann 1950), and the third term represents the radiation term. Thus, the non-zero rotation of the radiation force field always introduces the source term of magnetic field generation. It is worth noting that the gravitational force cannot be the source of magnetic field generation, since it is described by the gradient of a scalar potential.

We also mention that the final Equation (8) does not contain the terms directly originated from the electric current. In fact, Equation (8) is independent of conductivity, σ_c . The time derivative of magnetic field simply comes from Faraday's induction equation, i.e., the second equation of Maxwell Equation (6). Thus, the magnetic field generation by the radiation force in this paper can be regarded as the consequence of electromagnetic induction effects. The electric field with non-zero rotation is generated so as to cancel the radiation force. Thus, it is very natural that the second equation of Maxwell Equation (6) coincides with Equation (8), if we assume $e\mathbf{E} = \mathbf{f}_{\text{rad}}$ and neglect the advection term and Biermann term in Equation (8). We also note that a similar problem was considered in detail for the problem of field generation due to radiation forces in accretion disks around black holes (Bisnovatyi-Kogan & Blinnikov 1977; Contopoulos & Kazanas 1998; Bisnovatyi-Kogan et al. 2002; Contopoulos et al. 2006; Christodoulou et al. 2008).

Aside from the magnetic field generation described by Equation (8), we can assess the charge separation which drives the electric current. Taking the divergence of Equation (3) combined with the charge conservation Equation (5) and the first Maxwell Equation (6), we have

$$\frac{\partial \rho}{\partial t} + 4\pi\sigma_c\rho = \sigma_c \nabla \cdot \left(-\frac{1}{c} \mathbf{v} \times \mathbf{B} + \frac{1}{en_e c} \mathbf{j} \times \mathbf{B} - \frac{\nabla p_e}{en_e} + \frac{1}{e} \mathbf{f}_{\text{rad}} \right) \quad (9)$$

The second term on the left hand-side is much larger than the first term, since $1/(4\pi\sigma_c) \ll t$ is always satisfied. Therefore, the charge density is assessed as

$$\rho = \frac{1}{4\pi} \nabla \cdot \left(-\frac{1}{c} \mathbf{v} \times \mathbf{B} + \frac{1}{en_e c} \mathbf{j} \times \mathbf{B} - \frac{\nabla p_e}{en_e} + \frac{1}{e} \mathbf{f}_{\text{rad}} \right) \quad (10)$$

Thus, separated charge is piled up where the divergence of the force field is large. For instance, if we consider only \mathbf{f}_{rad} on the right-hand side of Equation (10), $\nabla \cdot \mathbf{f}_{\text{rad}}$ becomes negative in the neighborhood of the ionization front, since \mathbf{f}_{rad} changes very rapidly across the ionization front. Thus, electrons will accumulate around the ionization front.

2.2. Momentum transfer from radiation to electrons

In order to follow the generation of magnetic field, we need to evaluate the radiation force on electrons, \mathbf{f}_{rad} . Two elementary processes could be potentially important for this momentum transfer. First of all, Thomson scattering could contribute to \mathbf{f}_{rad} . We use the formal solution of the radiation transfer equation for $\mathbf{f}_{\text{rad,T}}$ as follows:

$$\mathbf{f}_{\text{rad,T}} = \frac{\sigma_T}{c} \int_0^{\nu_L} \mathbf{F}_{0\nu} d\nu + \frac{\sigma_T}{c} \int_{\nu_L}^{\infty} \mathbf{F}_{0\nu} \exp[-\tau_{\nu_L} a(\nu)] d\nu, \quad (11)$$

where $\mathbf{f}_{\text{rad,T}}$ denotes the radiation force per single electron due to Thomson scattering, σ_T is the cross section of Thomson scattering, $\mathbf{F}_{0\nu}$ is the unabsorbed energy flux density, ν_L denotes the Lyman-limit frequency, τ_{ν_L} is the optical depth at Lyman limit regarding the photoionization, and $a(\nu)$ denotes the frequency dependence of photoionization cross section, which is normalized at Lyman limit, i.e., $a(\nu_L) = 1$ is satisfied.

Second, the photoionization process itself also transfers the photon momentum to electrons. Its contribution to \mathbf{f}_{rad} is given as

$$\mathbf{f}_{\text{rad,I}} = \frac{1}{2} \frac{n_{\text{HI}}}{cn_e} \int_{\nu_L}^{\infty} \sigma_{\nu_L} a(\nu) \mathbf{F}_{0\nu} \exp[-\tau_{\nu_L} a(\nu)] d\nu, \quad (12)$$

where σ_{ν_L} denotes the photoionization cross section at the Lyman limit. We remark that the factor 1/2 in the right-hand side of Equation (12) is due to the fact that the photon momentum is equally delivered to protons and electrons. In fact, when electrons and protons are emitted by photoionization, its momentum is basically delivered to surrounding electrons and protons by Coulomb interaction. Since the number density and charge of each particle is the same for electrons and protons, electrons gain half of the momentum transferred from photons. Because of the large inertia of protons, we can also safely assume that only electrons are accelerated by this momentum transfer process.

The photoionization rate Γ in Equation (4) is also obtained by assuming the formal solution of the radiation transfer equation:

$$\Gamma = n_{\text{HI}} \int_{\nu_L}^{\infty} \sigma_{\nu_L} a(\nu) \frac{\mathbf{F}_{0\nu}}{h\nu} \exp[-\tau_{\nu_L} a(\nu)] d\nu \quad (13)$$

In practice, the photon conserving scheme (Abel, Norman & Madau 1999; Susa 2006) is used when we solve Equation (4), so that we can trace the propagation of the ionization front properly.

3. THE MODEL

3.1. Description of the model

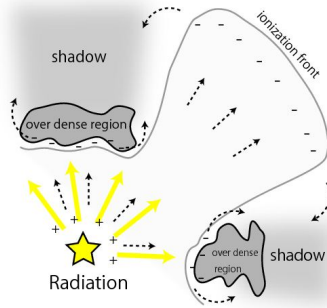


FIG. 1.— Schematic view of the magnetic field generation process. Dashed arrows represent the direction of electron flow.

We consider gas surrounding a first star. This ambient gas is ionized by the radiation from the source, forming an HII region. The momentum transfer from ionizing photons to electrons leads to a slight charge separation in the HII region. It creates a weak electric field balancing the radiation force.

The electric field and the distribution of charge cannot be isotropic, because the propagation speed of the ionization front is anisotropic due to the clumpiness of the surrounding media. As illustrated in Figure 1, overdense regions in the neighborhood of the radiation source form shadows behind themselves that result in anisotropic radiation flux as well as the electric field/charge distribution. Consequently, a transverse electric field along the ionization front is generated. This field could drive eddy currents surrounding the boundary between the shadowed and unshadowed regions. Thus, the magnetic field is expected to be generated at this boundary region.

3.2. Setup

We consider a first star of $500M_{\odot}$ ($L = 5 \times 10^{40} \text{ ergs}^{-1}$, $t_{\text{age}} = 2 \times 10^6 \text{ yr}$, $T_{\text{eff}} = 10^5 \text{ K}$ (Schaerer 2002)), at redshift $z \simeq 20$. Since the ionization front breaks out the small host halos with $M_{\text{halo}} \lesssim 10^7 M_{\odot}$ (Kitayama et al. 2004), we consider the expansion of the HII region in intergalactic space. The initial number density of the ambient gas in intergalactic space is $n_0 = 10^{-2} \text{ cm}^{-3}$ at such redshift. It is also assumed that the gas is neutral when the source star is turned on.

As shown in Figure 2, we follow the growth of magnetic flux density in a two-dimensional model. The computational domain is a strip of $500 \text{ pc} \times 5 \text{ kpc}$. The radiation flux flows from the left along the long edge of the domain. The assumed flux on the left edge is the flux 10 pc away from the source first star. We set an overdense region of $n_0 \text{ cm}^{-3}$, $D \text{ kpc}$ away from the left edge of the simulated region, which casts a shadow behind it (Figure 2). We tested four models A: $n_0 = 1 \text{ cm}^{-3}/D = 2 \text{ kpc}$, B: $n_0 = 1 \text{ cm}^{-3}/D = 200 \text{ pc}$, C: $n_0 = 10 \text{ cm}^{-3}/D = 200 \text{ pc}$, and D: $n_0 = 10 \text{ cm}^{-3}/D = 2 \text{ kpc}$. The overdense region has a core-halo structure. The diameter of the core ($n = n_0 \text{ cm}^{-3}$) is 50 pc , which is surrounded by the envelope of $n \propto r^{-2}$, where r is the radial distance from the center of the overdense region.

In this paper, we assume that the gas is isothermal ($T = 10^4 \text{ K}$), which results in eliminating the Biermann battery effect. In addition, we also assume that the gas is at rest, i.e. $\mathbf{v} = 0$. This assumption is valid when the ionization front is propagating in the intergalactic space; however, it is not appropriate in cases where the dense gas clump is photoevaporated because of the thermal pressure of the photoheated gas. These effects are left for future work. In this paper, we focus on the effects of radiation.

We also remark that the timescale for the ionization front to reach the Strömgren radius is $1/(\alpha n_e) \simeq 1.2 \times 10^7 \text{ yr}$ (Shu 1992), which is sufficiently longer than the lifetime of the source star. Therefore, the HII region does not settle down to a steady state during the lifetime of the source star (Yoshida et al. 2007).

4. RESULTS

4.1. Orders of magnitude

Before we move to the numerical results, it is useful to show the expected magnetic field strength by rough calculations. Following the isothermal and static fluid assumptions, Equation (8) is reduced to a very simple equation:

$$\frac{\partial \mathbf{B}}{\partial t} = -\frac{c}{e} \nabla \times \mathbf{f}_{\text{rad}} \quad (14)$$

This expression shows that the magnetic field is effectively generated where the radiation force field has a large shear. It is obvious that \mathbf{f}_{rad} should have a large derivative at the boundary between the shadowed and unshadowed regions. Thus, we focus our attention on such boundary region.

The radiation force \mathbf{f}_{rad} is assessed by Equations (11) and (12) as follows:

$$\mathbf{f}_{\text{rad}} = \mathbf{f}_{\text{rad,T}} + \mathbf{f}_{\text{rad,I}} \sim \frac{\mathbf{F}_0}{c} \left(\sigma_{\text{T}} + \frac{n_{\text{HI}}}{2n_{\text{e}}} \sigma_{\nu_{\text{L}}} \right), \quad (15)$$

where \mathbf{F} is the total energy flux coming from the source star. Thus, B is evaluated as

$$B \sim \frac{1}{e} \cdot \frac{1}{\Delta r} \cdot \frac{L_*}{4\pi R^2} \cdot \frac{1}{2} \sigma_{\nu_{\text{L}}} t_{\text{age}} \sim 10^{-18} \text{G} \left(\frac{\Delta r}{10 \text{pc}} \right)^{-1} \left(\frac{L_*}{5} \times 10^{40} \text{ergs}^{-1} \right) \left(\frac{R}{2 \text{kpc}} \right)^{-2} \left(\frac{t_{\text{age}}}{2 \times 10^6 \text{yr}} \right). \quad (16)$$

where Δr denotes the length scale that represents the sharpness of the boundary between the shadowed and unshadowed regions. Here we assume $n_{\text{HI}}/n_{\text{e}} \sim 1$ and the flux is not absorbed significantly ($F \sim L_*/(4\pi R^2)$). This assumption is only valid in the neighborhood of the ionization front. In the neutral region, dumping by the absorption of ionizing radiation reduces the radiation force. Therefore, Equation (16) should be regarded as an upper limit of the generated magnetic field strength.

It is also worth noting that Thomson scattering is negligible in neutral regions since the cross section is smaller than photoionization by 7 orders of magnitude, although it could be dominant in the highly ionized region. That is why the contribution from $\mathbf{f}_{\text{rad,T}}$ is omitted in Equation (16).

4.2. Numerical results

We integrate Equation (14) through the lifetime of the source star ($2 \times 10^6 \text{yr}$) after it turned on. Three snapshots for the distribution of magnetic field strength are shown in Figure3 for model A: $n_{\text{c}} = 1 \text{cm}^{-3}$, $D = 2 \text{kpc}$. Three panels correspond to 0.5, 1 and 2Myr after the ignition of the source star, from top to bottom, respectively. The radiation propagates from left to right in the panels, as the ionization front (green curve). The ionization front is trapped at the overdense core located 2kpc away from the left edge. Note that the right panels are compressed along the direction of the light rays, since the shadow is a quite elongated structure. The left panels have the same scale in both the horizontal and vertical directions.

The orange area denotes the region where the magnetic field is perpendicular to the plane of the page and directed to its front side. In the blue region, the magnetic field points in the opposite direction. First of all, it is clear that the magnetic field strength peaks at the boundary of the shadow cast by the dense core. As discussed in Section 4.1, \mathbf{f}_{rad} should vary significantly across the boundary between the shadowed and unshadowed regions, since the radiation flux is very weak in the shadow. In fact, as shown in Figure4, where the color contour of \mathbf{f}_{rad} is shown, \mathbf{f}_{rad} changes significantly behind the dense core. Since the ionization front is trapped at the dense core, the large shear of \mathbf{f}_{rad} is kept relatively long, while it is only transient in the low-density region far from the dense core. Thus, the magnetic flux density reaches its peak just behind the dense core, since it has enough time to grow.

We also remark that the border of the shadow does not coincide with the ionization front. As shown in Figure4, \mathbf{f}_{rad} is larger behind the ionization front, i.e., in the neutral region. This behavior indicates that the momentum transfer from photons to electrons through the photoionization process is more important than Thomson scattering since $\mathbf{f}_{\text{rad,I}}$ is larger in the neutral region, while Thomson scattering is important in the ionized region.

The time evolution of the peak magnetic field strength is plotted in Figure5. The field strength immediately reaches the level of $\sim 10^{-21} \text{G}$ after the ionization front hits the overdense region at $t = 2 \times 10^5 \text{yr}$. After that, the field strength grows gradually until the source star dies.

We also show three snapshots at 2Myr for three other models in Figure6. These panels correspond to models B, C and D from top to bottom, respectively.

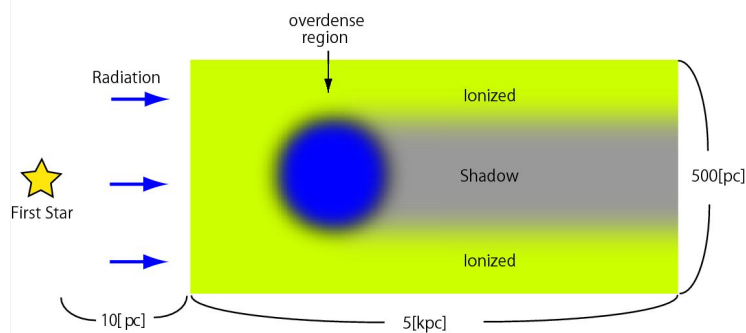


FIG. 2.— Schematic view of the computational domain. The shadowed region is formed behind the overdense region, while the other region is exposed to the radiation field.

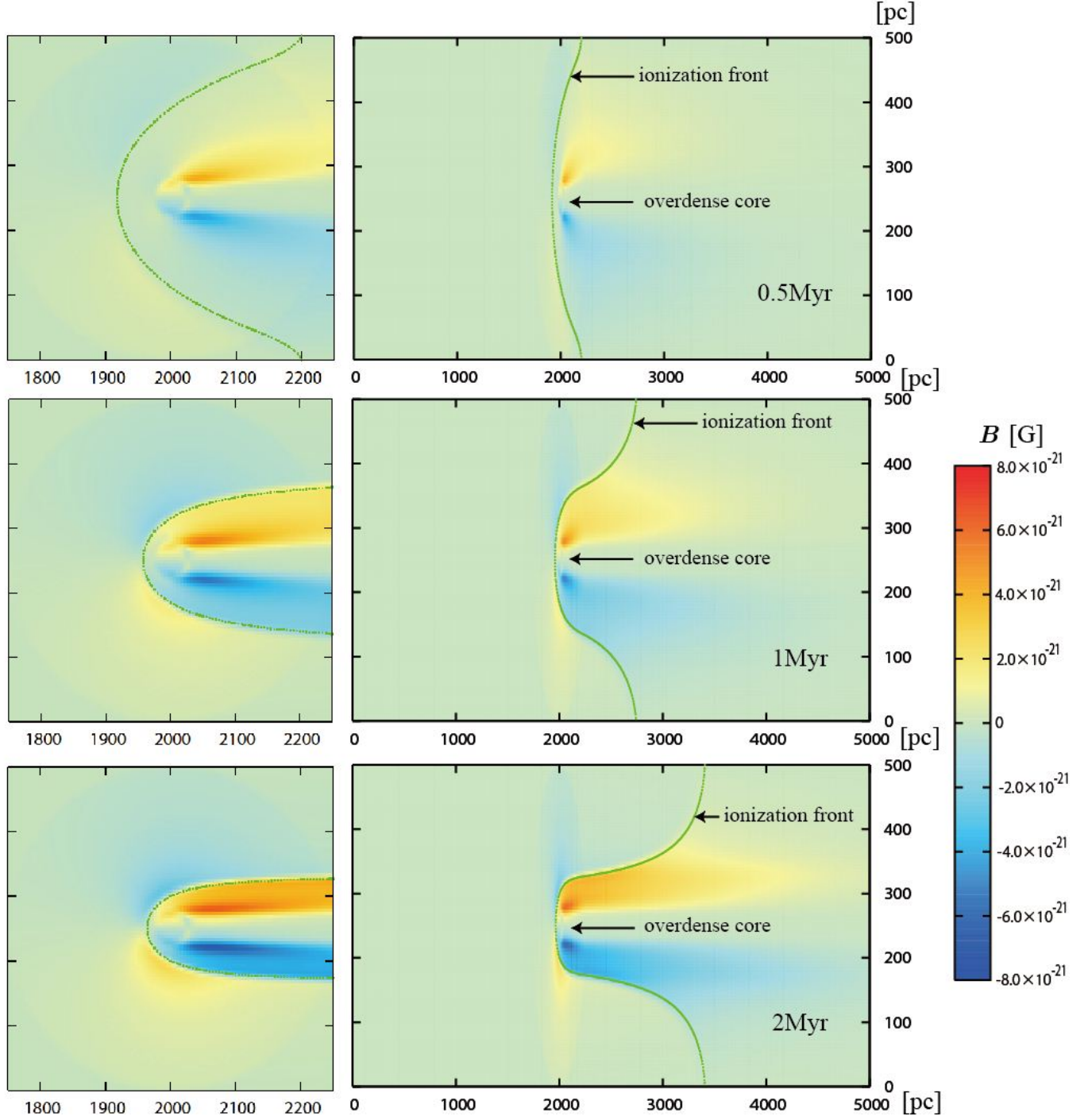


FIG. 3.— Color contour maps of the magnetic field strength at three snapshots at 0.5, 1 and 2 Myr. The three snapshots on the left are extended views around the dense core. Green lines denote the position of the ionization front. Orange represents the region in which B is directed to the front side of the page, whereas blue is used for the opposite direction.

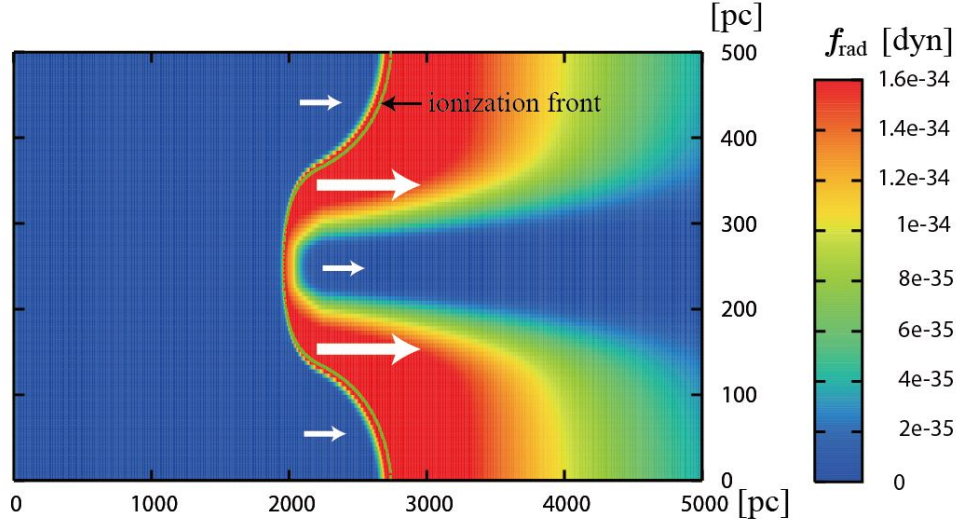


FIG. 4.— Color contour map of the radiation force f_{rad} 1Myr after the ignition of the source star. White arrows schematically show the flow of electrons.

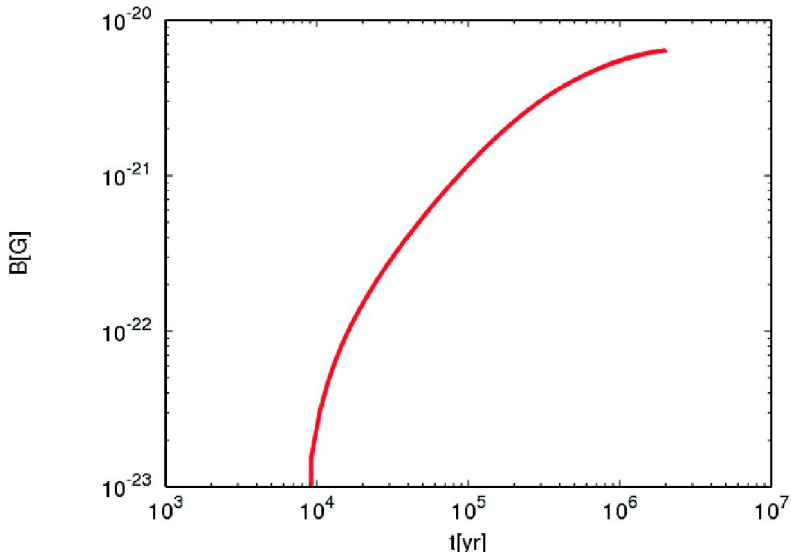


FIG. 5.— Time evolution of the peak magnetic field strength is plotted for model A: $n_c = 1\text{cm}^{-3}$, $D = 2\text{kpc}$.

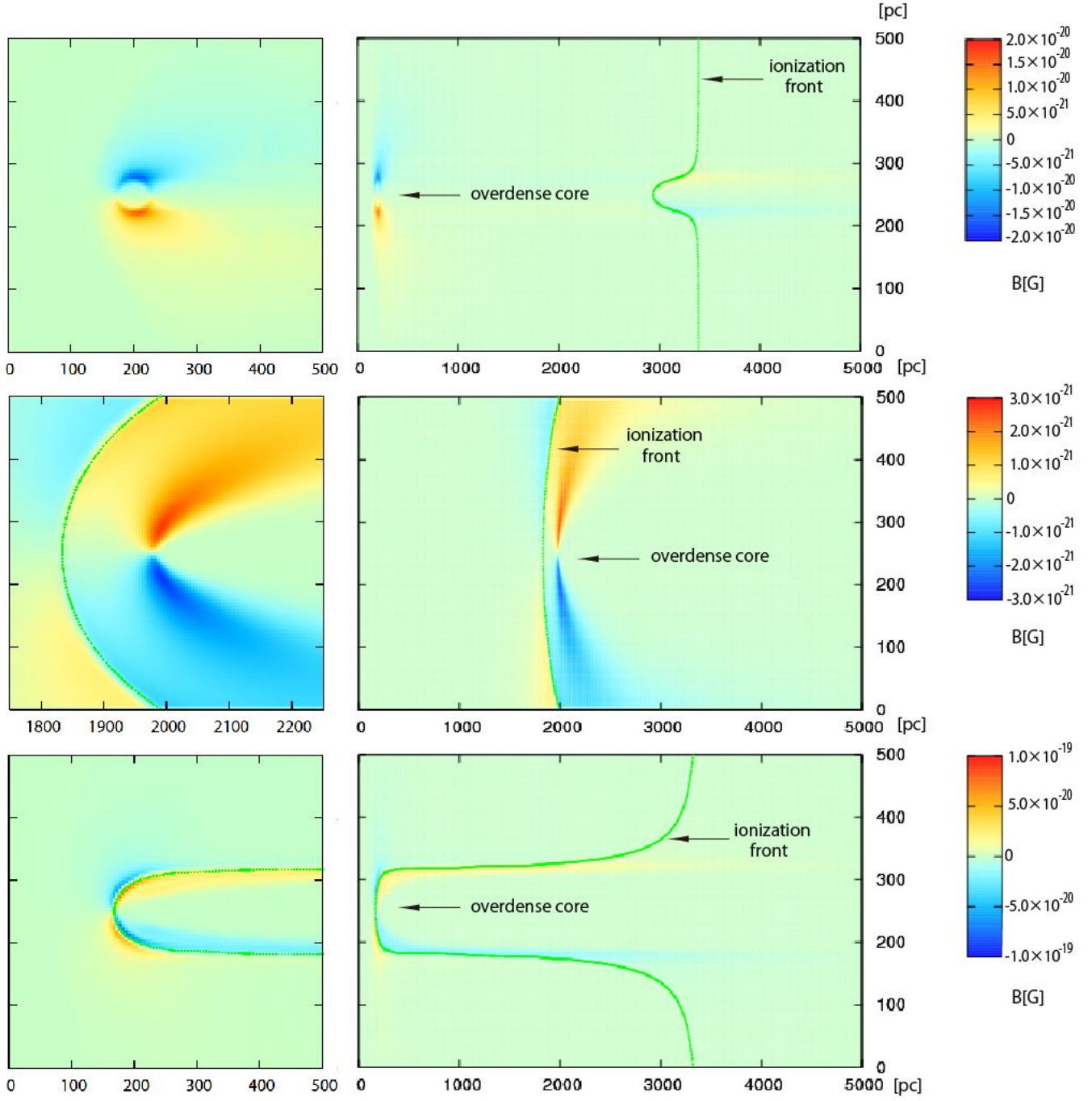


FIG. 6.— Color contour maps of the magnetic field strength at 2 Myr for model B: $n_c = 1 \text{ cm}^{-3}$, $D = 200 \text{ pc}$; model C: $n_c = 10 \text{ cm}^{-3}$, $D = 2 \text{ kpc}$; and model D: $n_c = 10 \text{ cm}^{-3}$, $D = 200 \text{ pc}$. The panels on the left represent extended views around the dense core. Green lines denote the position of the ionization front. Orange represents the region in which \mathbf{B} is directed to the front side of the page, whereas blue is used for the opposite direction.

In model B the dense core is located 10 times closer to the left edge than in the case of model A. We expect 100 times stronger magnetic field strength following the scaling relation of Equation (16). However, we have the maximum magnetic field strength of $\sim 2.0 \times 10^{-20}$ G. In this case, the ionization front is not trapped by the dense core. Consequently, the magnetic field does not have enough time to grow since the shadowed region behind the dense core is feathered after the ionization front passes through. Thus, the field strength does not follow the simple scaling relation.

Model C corresponds to the case where the density of the core is 10 times larger than that in model A, while the distance D is the same. The peak magnetic field strength in this model is as large as 3.0×10^{-21} G, which is smaller than the case of model A by a factor of few. Since the ionization front does not pass through even at the envelope of the overdense region, the rotation of \mathbf{f}_{rad} (i.e., the shear of \mathbf{f}_{rad}) around the dense core becomes relatively smaller than that in model A. Therefore, the magnetic field strength is smaller than the case of model A.

Finally, we describe the results of model D, which are shown in the bottom panels of Figure 6. In model D, the core is located 10 times closer, and is 10 times denser than that in model A. As shown in Figure 6, the ionization front is trapped in front of the dense core because of the high enough core density. It is also clear that the ionizing radiation flux is high enough to ionize the envelope, unlike model C. In this case, the maximal magnetic field strength is $\sim 10^{-19}$ G.

The parameters employed in models A to D scan the reasonable range. In fact, the actual size of the HII region of a $500M_{\odot}$ first star is as large as several kpc, and the size of the first halos is $\lesssim 100$ pc. The density of the virialized halo is $\sim 1\text{cm}^{-3}$ at $z = 20$. Thus, we can conclude that the magnetic flux density generated by radiation from first stars is $\lesssim 10^{-19}$ G.

5. DISCUSSION

We found that the generated magnetic field strength is $\sim 10^{-19}$ G at maximum if we adopt reasonable ranges for the parameters in our model. This value is much smaller than those predicted by steady theory (Langer et al. 2003), although we take into account the additional contribution by $\mathbf{f}_{\text{rad},\text{I}}$. If we consider only Thomson scattering as done in Langer et al. (2003), we obtain a magnetic field of $\sim 10^{-25}$ G. This discrepancy comes from the steady assumption. In their study, the magnetic field strength was estimated using steady equations, however; as shown in Section 2.1, a much longer time than the age of the universe is needed to settle down to steady state in this situation. Considering a realistic timescale, such as the age of the source star $\sim 10^6$ yr, we conclude that the steady assumption is wrong.

In the present work, the system is assumed to be isothermal ($= 10^4$ K) for simplicity, which results in eliminating the Biermann battery term. In a more realistic situation, we have to consider the effects of radiation hydrodynamics as well as the heating and cooling of gas by which we can compute the magnetic field generated by the battery effect (Biermann 1950). In fact, the order of magnitude of magnetic field generated by the battery effect is

$$B \sim \frac{c}{n_e^2 e} \left(\frac{n_e}{\Delta r} \right) \left(\frac{p_e}{\Delta r} \right) \sin \theta t_{\text{age}} \sim 2.0 \times 10^{-18} \left(\frac{t}{2.0 \times 10^6 \text{ yr}} \right) \left(\frac{\sin \theta}{0.1} \right) \left(\frac{\Delta r}{10 \text{ pc}} \right)^{-2} \left(\frac{T}{10^4} \right) \text{ G}, \quad (17)$$

where Δr denotes the typical length of n_e and p_e change significantly and θ denotes the angle between ∇n_e and ∇T . This expected field strength is even larger than the flux density due to radiation pressure, although we have significant uncertainties in the above estimate. Thus, we need to include the Biermann battery term to assess the correct magnetic field strength utilizing radiation hydrodynamic calculations, which is left for future work.

We also remark that the magnetic field strength obtained in this paper seems insufficient to affect star formation in the early universe, since $B \sim 10^{-19}$ G at IGM cannot account for 10^{-10} to 10^{-9} G at $n = 10^3 \text{cm}^{-3}$ required for jet formation (Machida et al. 2006) and MRI activation (Tan & Blackman 2004). However, it is also worth noting that a very recent study by Schleicher et al. (2010) indicates that turbulence in the host halos of first stars (e.g., Wise & Abel 2008) can amplify the magnetic field to equipartition strength very quickly. If this is true, this might suppress the fragmentation of gas disks formed at the center of the star-forming gas (Machida et al. 2008), and help the MRI activation.

6. CONCLUSION

We investigate the magnetic field generation process by radiation force in a nonlinear and unsteady framework along the line of the theory of Langer et al. (2003). We consider a specific model of magnetic field generation around a very massive first star. Using analytical and numerical calculations, we find that the steady assumption is not valid in realistic situations and obtain a much smaller magnetic field strength than predicted by the steady theory. In addition, we find that the momentum transfer process during photoionization is more important than Thomson scattering. The resultant magnetic flux density around first stars is $\sim 10^{-19}$ G. This seed magnetic field does not seem to affect subsequent star formation in the neighborhood of first stars.

We thank the anonymous referee for critical comments which helped to improve the manuscript. We also thank N. Tominaga for fruitful discussions. This work was supported in part by the Inamori Foundation, as well as Ministry of Education, Science, Sports and Culture, Grant-in-Aid for Scientific Research (C), 22540295.

REFERENCES

- Abel T., Norman M. L., & Madau P., 1999, *ApJ*, 523, 66
- Abel, T., Bryan, G. L., & Norman, M. L. 2002, *Science*, 295, 93
- Biermann, L. 1950, *Zs. Naturforsch.*, 5a, 65
- Bisnovatyi-Kogan, G. S., & Blinnikov, S. I. 1977, *A&A*, 59, 111
- Bisnovatyi-Kogan, G. S., Lovelace, R. V. E., & Belinski, V. A. 2002, *ApJ*, 580, 380
- Bisnovatyi-Kogan, G. S., Ruzmaikin, A. A., & Syunyaev, R. A. 1973, *Sov Astron*, 17, 137
- Bromm, V., Coppi, P. S., & Larson, R. B. 2002, *ApJ*, 564, 23
- Christodoulou, D. M., Contopoulos, I., & Kazanas, D. 2008, *ApJ*, 674, 388
- Contopoulos, I., & Kazanas, D. 1998, *ApJ*, 508, 859
- Contopoulos, I., Kazanas, D., & Christodoulou, D. M. 2006, *ApJ*, 652, 1451
- Shu, F.H. 1992, *Gas Dynamics*(Mill Valley, CA: Univ. Science Books)
- Gnedin, N.Y., Ferrara, A., & Zweibel, E.G. 2000, *ApJ*, 539, 505
- Harrison, E. R. 1970, *MNRAS*, 147, 279
- Ichiki, K., Takahashi, K., Ohno, H., Hanayama, H., & Sugiyama, N. 2006, *Science*, 311, 8271
- Kitayama, T., Yoshida, N., Susa, H., & Umemura, M. 2004, *ApJ*, 613, 631
- Lang, K.R. 1999, *Astrophysical Formulae*(New York: Springer)
- Langer, M., Puget, J., & Aghanim, N. 2003, *Phys. Rev D*, 67, 43505
- Machida, M.N., Omukai, K., Matsumoto, T., Inutsuka, S. 2006, *ApJ*, 647, L1
- Machida, M. N., Matsumoto, T., & Inutsuka, S.-i. 2008, *ApJ*, 685, 690
- Maki, H., & Susa, H. 2004, *ApJ*, 609, 467
- Maki, H., & Susa, H. 2007, *PASJ*, 59, 787
- Mishustin, I.N., & Ruzmaikin, A. A. 1972, *Sov J. Exp Theor Phys*, 34, 233
- Nakamura, F., & Umemura, M. 2001, *ApJ*, 548, 19
- Omukai, K., Tsuribe, T., Schneider, R., & Ferrara, A. 2005, *ApJ*, 626, 627
- Schneider, R., Ferrara, A., Salvaterra, R., Omukai, K., & Bromm, V. 2003, *Nature*, 422, 869
- Shapiro, P.R., & Giroux, M.L. 1987, *ApJ*, 321, L107
- Schleicher, D. R. G., Galli, D., Glover, S. C. O., Banerjee, R., Palla, F., Schneider, R., & Klessen, R. S. 2009, *ApJ*, 703, 1096
- Schleicher, D. R. G., Banerjee, R., Sur, S., Arshakian, T. G., Klessen, R. S., Beck, R., & Spaans, M. 2010, *arXiv:1003.1135*
- Schaerer, D. 2002, *A&A*, 382, 28
- Susa, H. 2006, *PASJ*, 58, 445
- Tan, J. C., & Blackman, E. G. 2004, *ApJ*, 603, 401
- Turner, M.S., & Widrow, L.M. 1988, *Phys. Rev.D*, 37, 2743
- Wise, J. H., & Abel, T. 2008, *ApJ*, 685, 40
- Xu, H., O'Shea, B., Collins, D., Norman, M., Li, H., & Li, S. 2008, *ApJ*, 688, L57
- Yoshida, N. 2006, *New Astron Rev*, 50, 19
- Yoshida, N., Oh, S. P., Kitayama, T., & Hernquist, L. 2007, *ApJ*, 663, 687